NeuroImage 192 (2019) 135–144

Contents lists available at ScienceDirect

NeuroImage

journal homepage: www.elsevier.com/locate/neuroimage

In vivo neurovascular response to focused photoactivation of Channelrhodopsin-2

James R. Mester [a,b,*], Paolo Bazzigaluppi [b], Iliya Weisspapir [b], Adrienne Dorr [b], Tina L. Beckett [b], Margaret M. Koletar [b], John G. Sled [a,c], Bojana Stefanovic [a,b]

[a] University of Toronto, Department of Medical Biophysics, Toronto, Ontario, Canada
[b] Sunnybrook Research Institute, Toronto, Ontario, Canada
[c] Mouse Imaging Centre, The Hospital for Sick Children, Toronto, Ontario, Canada

ARTICLE INFO

Keywords:
Two-photon fluorescence microscopy
Neurovascular coupling
Optogenetics
Thy1-ChR2

ABSTRACT

The rapid growth in the use of optogenetics for neuroscience applications is largely driven by two important advantages: highly specific cellular targeting through genetic manipulations; and precise temporal control of neuronal activation via temporal modulation of the optical stimulation. The difference between the most commonly used stimulation modalities, namely diffused (i.e. synchronous) and focused (i.e. asynchronous) stimulation has not been described. Furthermore, full realization of optogenetics' potential is hindered by our incomplete understanding of the cellular and network level response to photoactivation. Here we address these gaps by examining the neuronal and cerebrovascular responses to focused and diffuse photostimulation of channelrhodopsin in the Thy1-ChR2 mouse. We presented the responses of photoactivation via 470-nm fiber optic illumination (diffuse) alongside 458-nm raster-scan (focused) stimulation of the barrel field. Local field potentials (LFP) assessment of intracerebral electrophysiology and two-photon fluorescence microscopy measurements of red blood cell (RBC) speed (v_{RBC}) in cortical penetrating vessels revealed ~40% larger LFP responses ($p = 0.05$) and twice as large cerebrovascular responses ($p = 0.002$) under focused vs. diffuse photostimulation (focused: 1.64 ± 0.84 mV LFP amplitude and $75 \pm 48\%$ increase in v_{RBC}; diffuse: 1.14 ± 0.75 mV LFP amplitude and $35 \pm 23\%$ increase in v_{RBC}). Compared to diffuse photostimulation, focused photostimulation resulted in a ~65% increase in the yield of cerebrovascular responses ($73 \pm 10\%$ for focused and $42 \pm 29\%$ for diffuse photostimulation) and a doubling of the signal-to-noise ratio of the cerebrovascular response (20.9 ± 14.7 for focused and 10.4 ± 1.4 for diffuse photostimulation). These data reveal important advantages of focused optogenetic photoactivation, which can be easily integrated into single- or two-photon fluorescence microscopy platforms, as a means of assessing neuronal excitability and cerebrovascular reactivity, thus paving the way for broader application of optogenetics in preclinical models of CNS diseases.

1. Introduction

Light stimulation provides two major advantages over other means of neuronal modulation (e.g. electrical stimulation): higher spatio-temporal control of the stimulation and the capability to target specific neuronal subpopulations through genetic manipulation or viral transfection. Extensive work has characterized the effects of opsins photoactivation on individual neuronal firing or population neuronal firing in vitro and in vivo (Arenkiel et al., 2007). Photoactivation, with 450–480 nm light, of Channelrhodopsin-2 (ChR2), the most widely used opsin, (C. K. Kim et al., 2017; Nagel et al., 2003; Boyden et al., 2005; Zhang et al., 2006), results in rapid neuronal membrane depolarization (Nagel et al., 2005), and action potential generation for light pulses longer than 10 ms (in transfected hippocampal neurons cell-cultures (Boyden et al., 2005)). While temporal modulation of ChR2 photoactivation has been widely utilized, spatial focusing of the photostimulation holds great potential but is currently underutilized, especially in the study of the neurovascular coupling and its cellular origins (Ayling et al., 2009; Scott and Murphy, 2012; Wilson et al., 2013; Cheng et al., 2014; Iordanova et al. 2015, 2018; Anenberg et al., 2015; Richner et al., 2015; Uhlirova et al., 2016; Rungta et al., 2017; Bauer et al., 2018; Vazquez et al., 2014), which is now recognized as key for understanding brain (dys)function (Davis

* Corresponding author. Sunnybrook Health Sciences Centre, 2075 Bayview Ave., S636, Toronto, ON, M4N 3M5, Canada.
E-mail address: james.mester@mail.utoronto.ca (J.R. Mester).

https://doi.org/10.1016/j.neuroimage.2019.01.036
Received 12 October 2018; Received in revised form 31 December 2018; Accepted 14 January 2019
Available online 19 January 2019
1053-8119/

et al., 1998; Dirnagl et al., 1999; Attwell and Iadecola, 2002; Lauritzen, 2005; Iadecola, 2017).

Two modalities of light stimulation are used, which differ substantially due to engineering (i.e. how the light is generated and delivered) and biology (i.e. how neurons react to the different simulation). In the first modality, light generated by an LED is delivered by an optic fibre and is henceforth referred to as *diffuse photostimulation;* in the second, pulsed laser light is focused by the microscope objective and raster-scanned over a portion of the brain, here termed *focused photostimulation*. The differences underlying the two approaches have not been fully examined. Diffuse stimulation illuminates the whole surface of brain exposed by the craniotomy (e.g. $\sim 2 \times 2 mm^2$) resulting in simultaneous activation of ChR2 expressing neurons (Iordanova et al., 2015). Light pulses (of e.g. 10-millisecond duration) spaced by intervals of constant duration (e.g. 50 ms) entrain the pyramidal neurons in a periodic and synchronized excitatory wave that overrides the physiological balance between excitation and inhibition. Focused stimulation, on the other hand, relies on a continuous wave laser which raster scans over a region of interest 2–3 orders of magnitude smaller than the one exposed by the craniotomy. Galvanometers drive the light beam across all the pixels in a Cartesian grid with a cycle duration driven by pixel dwell time and the size of the photostimulation region. Blue light at the power generated by a laser ($2–4 mW/mm^2$) penetrates effectively (i.e. with power necessary to elicit a response) down to hundreds of micrometers (Al-Juboori et al., 2013). Single photon light focused at 150 μm excites, with its cone of light, the column of tissue above the focal plane. This scanning approach results in sequential and periodic illumination across the cone of tissue above the photostimulation area in the focal plane, and hence synchronous neuronal activation within a cone yet asynchronous neuronal activation across the ROI (for this reason the term "stimulation frequency" would be confusing and is not used). This stimulation is spatially more confined and recruits 2–3 orders of magnitude fewer neurons than does the diffuse stimulation.

Our current work aims to assess focused photostimulation for the study of neurovascular coupling and provide recommendations for its informed use. We characterized the coupling of blood flow through individual cortical penetrating vessels and pyramidal neurons' activation elicited by ChR2 photostimulation. We imaged a cohort of Thy1-ChR2 mice expressing ChR2 in pyramidal neurons and their non-transgenic controls on a two-photon fluorescence microscope to quantify the amplitude and kinetics of red blood cell velocity in cortical penetrating vessels following focused (via 458 nm laser raster-scanning) photostimulation (PS) or diffuse (via 470 nm fibre-coupled LED) PS and characterized the evoked local field potentials via intracerebral electrophysiological recordings. The findings reveal significant advantages of focused photostimulation for in vivo studies of neurovascular coupling.

2. Methods

2.1. Animals

All experimental procedures in this study followed the ARRIVE guidelines and were approved by the Animal Care Committee of the Sunnybrook Research Institute, which adheres to the Policies and Guidelines of the Canadian Council on Animal Care and meets all the requirements of the Provincial Statute of Ontario, Animals for Research Act as well as those of the Canadian Federal Health of Animals Act. Thirty-four adult male and female Thy1-ChR2-YFP mice (with expression of wild-type strain of ChR2 in excitatory pyramidal neurons, strain number 007615, line 9 (Arenkiel et al., 2007), Jackson Laboratory) were bred in-house for these experiments (thirty for 2PFM experiments, four for electrophysiology experiments) at the age of 3–6 months. Eleven age-matched male and female C57BL/6 mice were used in control experiments (six for 2PFM experiments, five for electrophysiology experiments). Cohort sizes and attrition rates are summarized in Table 1.

Table 1
Outline of animal usage and attrition (due to surgical complications, poor physiological condition, etc.) by experiment, mouse line, and sex. Total numbers assigned were based on sex availability from in-house breeding.

Experiment	Mouse line	Sex	Total	Attrition	Final
2PFM	Thy1-ChR2	M	18	2	16
		F	12	3	9
	C57BL/6	M	3	0	3
		F	3	0	3
Electrophysiology	Thy1-ChR2	M	4	0	4
		F	2	0	2
	C57BL/6	M	2	0	2
		F	3	0	3

2.2. Surgical preparation

Mice were induced under 5% isoflurane and then moved to a feedback-controlled temperature pad (CWE Inc, Ardmore, PA) where they were maintained at 37°C under 2–2.5% isoflurane. They were then tracheostomized for mechanical ventilation (SAR 830/P, CWE Inc.) and the tail vein was cannulated for fluorophore injection and subsequent alpha-chloralose delivery. Throughout the experiments, systemic physiology was monitored with a pulse oximeter (MouseOx, STARR Life Sciences) for recording of breath rate, heart rate, arterial oxygen saturation, and pulse and breath distention using a Biopac amplifier (Biopac Systems Canada).

Following tracheostomy, anesthesia level was lowered to 1–1.5% isoflurane and mice were fixed on a stereotactic frame for immobilization via incisor bar and ear bars. Ringer's lactate solution (130 mmol/L Na, 4 mmol/L K, 1.5 mmol/L Ca, 109 mmol/L Cl, 28 mmol/L lactate, 0.5–1 mL volume, Hospira, Canada) and Xylocaine (10 mg/mL, 50–100 μL volume, AstraZeneca Canada, Canada) were administered subcutaneously for hydration and local anesthesia, respectively. Cranial window installation was performed following established procedures (Dorr et al., 2012). A dental drill was used to create a 2–3 mm craniotomy centered over the whisker-barrel cortex (-1 mm AP, +3.5 mm ML). The skull cap was removed and the dura left intact. 1% agarose in phosphate-buffered saline (PBS) (Sigma-Aldrich) was applied to the dura shortly prior to placement of a 5 mm glass cover slip over the craniotomy. The cover slip was then secured with cyanoacrylate glue and an immersion well surrounding the cranial window created with dental cement (Land Dental, USA). A 70 kDa Texas Red dextran (Invitrogen, USA) dissolved in PBS (8.33 mg/mL) was administered via the tail vein (25 mg/kg body weight).

2.3. Two-photon fluorescence imaging (2PFM) and optogenetic stimulation

Mice were imaged on an FVMPE-RS multiphoton microscope (Olympus, Japan) using a 25x/1.05NA objective lens (Olympus, Japan). After positioning the mouse under the microscope, the anesthesia was switched to intraveneous alpha-chloralose (100 mg/kg induction, 40 mg/kg/hr maintenance) delivered by an infusion pump (Harvard Apparatus, USA). An Insight Ti:Sapphire laser (SpectraPhysics, USA) tuned to 900 nm was used to image Texas Red-labelled vasculature and YFP-labelled ChR2-expressing pyramidal neurons. Two PMTs aligned with barrier filters (485–540 nm and 575–630 nm) and separated by a 570 nm dichroic mirror (Chroma Technology, USA) were used for simultaneous detection of fluorophores. Raster scanned visible wavelength lasers (458nm/552 nm) were used for focused photostimulation (PS) with separate galvanometers for simultaneous 2PFM imaging and visible photostimulation. Line scanning (1.1–1.3 ms/line, 2μs/pixel) along longitudinal axes of vessels was accompanied by raster scan photostimulation over a circular area of a diameter given by the average inter-penetrating vessel distance as estimated from morphological 2PFM data in Thy1-ChR2 mice ($2–4 mW/mm^2$, raster-scanned photostimulation over 130 μm diameter circular ROI, 551 ms repetition period,

4μs/pixel, 2–5.5s duration). To allow characterization of this photostimulation paradigm in reference to conventional photostimulation, a fiber-coupled 470 nm LED (built in-house) was used for diffuse PS (2–8 mW/mm^2, 20Hz, 10 ms pulse length, 5s duration) (Fig. 1). Photostimulation power was measured via power meter (Model 842-PE, Newport, USA). Power density conversion was performed using the area of the stimulation ROI (130 μm diameter circular ROI) for focused PS and using an empirical model of light propagation in mammalian brain tissue provided by the Deisseroth lab (https://web.stanford.edu/group/dlab/cgi-bin/graph/chart.php) for diffuse PS. Laser power density was not matched between the two conditions because the power density of fibre-delivered stimulation, when applied to focused stimulation, resulted in persistent RBC speed elevations for minutes after offset of focal stimulation. Conversely, at low power densities of the fibre-delivered stimulus, the RBC speed changes were found irreproducible. We ultimately used power of the fibre-delivered stimulation typical of levels used in the literature (G.-Y. Wu et al., 2015; Jennings et al., 2013; Lammel et al., 2012; Iordanova et al., 2015; Anenberg et al., 2015) and optimized the focal stimulus power density to maximize response yield within appropriate power levels and expedite the return to baseline.

2.4. Electrophysiological recordings

In separate experiments, local field potentials (LFPs) were recorded in response to optogenetic and whisker stimuli. Mice were prepared as for the imaging experiments, but the coverslip was not installed. Brain surface was kept moist with PBS-soaked Surgifoam (Ferrosan Medical Devices, Denmark). A pulled pipette microelectrode was prepared and the tip placed just under the pial surface of the exposed brain over the whisker-barrel cortex (-1 mm AP, +3.5 mm ML). LFP signal was recorded using an EPC-10 Heka amplifier (HEKA, Germany). LFP recordings were made in response to diffuse (8 mW/mm^2, 20Hz, 10 ms pulse length, 5s duration) and focused (2–4 mW/mm^2, 130 μm stimulus ROI diameter, 551 ms repetition rate, 4μs/pixel, 2–5.5s duration) PS as well as a whisker puff stimulus (50-ms air puffs at 10Hz, for 5s) via Picospritzer (Parker Hannifin, Hollis, NH).

2.5. RBC speed estimation

Linescan analysis was adapted from previous work by (T. N. Kim et al., 2012). Briefly, line-scanning particle image velocimetry (LS-PIV) allows for recording of noisy data on fast moving red blood cells (RBCs) such as those in cortical penetrating vessels. This method applies a cross-correlation to sequential linescans to capture RBC speed (v_{RBC}) information from more cells when compared to conventional methodology (Kleinfeld et al., 1998), providing more accurate RBC speed estimation in higher-flow vessels. Linescan data were collected via 2PFM imaging with 900 nm excitation of Texas Red-containing plasma in penetrating vessels at their diving point, as shown in Fig. 1c. 2D X-T images were generated from repeated linescans (Fig. 1d). 2D linescan images were corrected for DC offset during image acquisition and 1D Fast Fourier transform (FFT) of each line computed for cross-correlation calculations. 1D FFTs were multiplied by adjacent lines and the inverse FFTs of the product taken to compute the cross-correlation. Gaussian peak-fitting was performed on the cross-correlations to determine the spatial shift of RBCs between adjacent lines and the time for acquisition of a single linescan used in conjunction with the spatial shifts to calculate v_{RBC} (Fig. 1e).

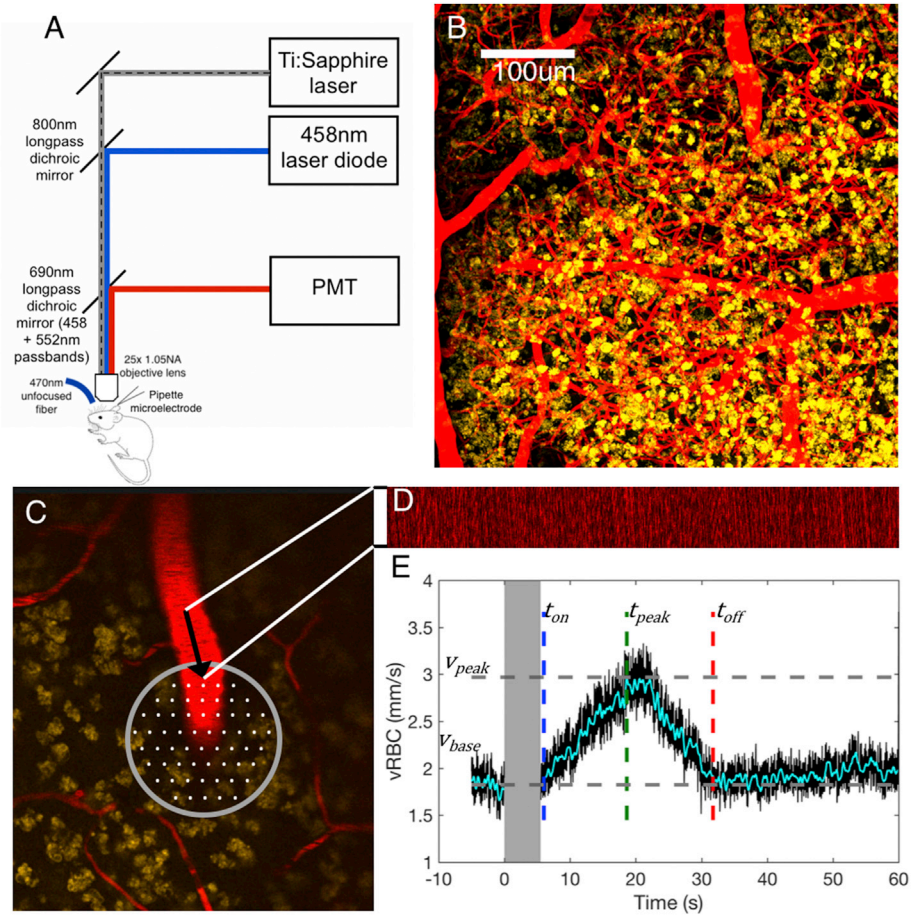

Fig. 1. Experimental setup. A. Schematic diagram of beam-combining optics for simultaneous 2PFM and optogenetic photostimulation (PS) and pipette microelectrode for electrophysiology experiments. B.Maximum-intensity projection of 2PFM image acquired in the barrel cortex of Thy1-ChR2-YFP mice. Yellow: pyramidal neurons expressing ChR2-YFP. Red: Texas Red-labeled plasma of cerebral vasculature. C. 2P XY image displaying a diving point of a penetrating cerebral vessel. Gray: ROI of raster-scan optogenetic stimulation at 458 nm, centered over penetrating vessel. Black arrow: linescan trajectory. White points: representative pattern of pixelwise raster-scan photostimulation. D. Example raw linescan data recording fluorescence of Texas Red-labeled plasma at 900 nm. Black streaks are created by RBC passage. E. RBC speed estimates vs. time before (black) and after (cyan) median filtering. Blue box indicates stimulus period. Dotted lines indicate aparametrically estimated onset time (t_{on}), peak time (t_{peak}) and offset time (t_{off}).

2.6. Calculation of v_{RBC} and LFP kinetic parameters

Scripts for evaluation of v_{RBC} and LFP response kinetics were written in MATLAB (Mathworks, Natick, MA). To minimize the effects of respiratory and pulmonary fluctuations as well as random noise on v_{RBC}, traces were median filtered in time and a 10-point moving average was applied. To establish presence of a v_{RBC} or LFP response to stimulation, a variance ratio test was performed on the ratio between the v_{RBC} or LFP variance during the 5s pre-stimulus baseline vs. those during the 30s following stimulus onset. Only traces showing statistically significant increase (p *0.05)* in the variance post-vs. pre-stimulus were analyzed further. Next, post-stimulus recordings were z-scored (z_V) using the mean and standard deviation of the 5s pre-stimulus baseline recording. Post-stimulus LFP or v_{RBC} recordings that did not contain a continuous period of $z_V \geq 2$ longer than the stimulus duration (LFP) or 5s (v_{RBC}) were excluded from the analysis. (Five second interval was selected as the minimum cerebrovascular response period based on our stimulus parameters and the responses seen with comparable stimuli in published reports of rodent cortical vascular responses (Kleinfeld et al., 1998; Uhlirova et al., 2016; Anenberg et al., 2015; Hill et al., 2015; Rungta et al., 2017; Iordanova et al., 2015, 2018; Cheng et al., 2014) Responses that met these criteria were further parametrized. Onset time (t_{onset}) was defined as the first point in time post-stimulus at which $z_V \geq 2$ (i.e. where v_{RBC} or LFP is 2 SDs above the pre-stimulus baseline). Similarly, off time (t_{off}) denoted the time at which the continuous period of $z_V \geq 2$ ended. We considered response duration to be the time between t_{onset} and t_{off}. Within the response duration, we computed multiple absolute and relative (to pre-stimulus baseline) parameters: absolute and relative peak response amplitude ($\Delta v_{RBC\ peak}$ for v_{RBC} responses, peak LFP amplitude for LFP responses), absolute and relative average response amplitude ($\Delta v_{RBC\ avg}$, v_{RBC} responses only), time-to-peak (t_{peak}, time from stimulus onset to $v_{RBC\ peak}$), and absolute and relative acceleration (v_{RBC} responses only) defined as

$$a_{RBC} = \frac{\Delta v_{RBC\ peak}}{t_{peak} - t_{onset}}$$

2.7. Statistical methods

Parameter estimates were analyzed in R software (The R Foundation). As these data were not normally distributed on Shapiro-wilk test, the Wilcoxon rank sum test was used in their statistical analysis. Standard deviation (SD) was used to report uncertainty.

3. Results

3.1. Cerebrovascular response to focused photostimulation

The experimental set-up along with a sample maximum intensity projection 2PFM image in a Texas Red dextran-injected thy1-ChR2 mouse is shown in Fig. 1. In light of recent reports on commonly-used optogenetic stimulation inducing a cerebrovascular response in the absence of optogenetic actuators (Christie et al., 2013; Rungta et al., 2017), we performed a series of control experiments. Fig. 2a compares the average cerebrovascular responses to focused PS in a Thy1-ChR2 (TG) mouse to those in a non-transgenic littermate (nTG) mouse. The TG mouse shows a prominent cerebrovascular response to stimulation whereas no fluorescence changes in response to focused PS were

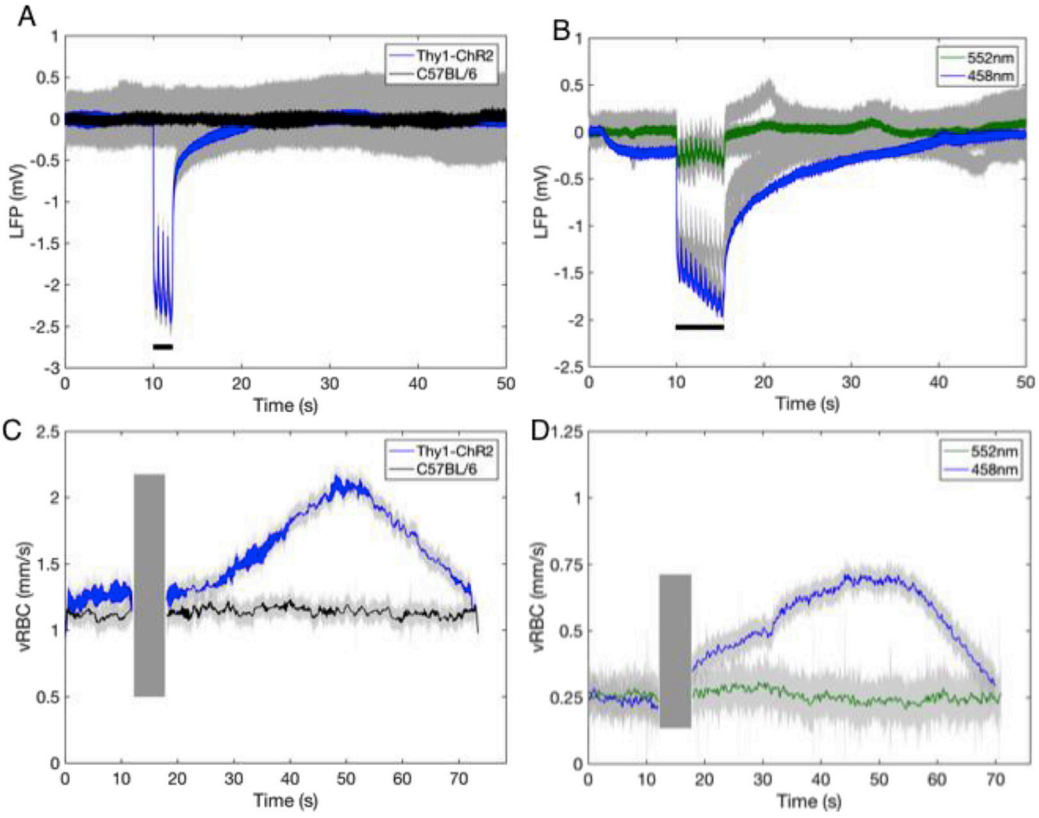

Fig. 2. Neuronal and cerebrovascular responses specificity to blue light optogenetic photostimulation. A. Comparison of local field potential (LFP) recordings in thy1-ChR2 and C57BL/6 mice in response to 458 nm local focused photostimulation (PS) (3 mW/mm^2, 130 μm stimulus ROI diameter, 551 ms repetition rate, 4μs/pixel). Gray depicts individual traces, black and blue traces indicate average response to repeated stimuli. Black bar indicates duration of stimulus delivery. B. Comparison of local field potential (LFP) recordings in thy1-ChR2 mice in response to power-matched 458 nm (blue) and 552 nm (green) local focused photostimulation (PS) (3 mW/mm^2, 130 μm stimulus ROI diameter, 551 ms repetition rate, 4μs/pixel). Gray depicts individual traces and blue/green traces indicate average response to repeated stimuli. Black bar indicates duration of stimulus delivery. C. Comparison between arteriolar average v_{RBC} responses to 458 nm local focused PS (3 mW/mm^2, 130 μm stimulus ROI diameter, 551 ms repetition rate, 4μs/pixel) in thy1-ChR2 and C57BL/6 mice. Dark gray box depicts stimulus duration, light gray indicates 95% CI of LSPIV v_{RBC} estimate. D. Comparison between venular average v_{RBC} responses to power-matched 458 nm (blue) and 552 nm (green) local focused photostimulation (PS) (3 mW/mm^2, 130 μm stimulus ROI diameter, 551 ms repetition rate, 4μs/pixel).

observed in the nTG animal. Across repeated focused PS in 48 different vessels in 6 nTG mice, no cerebrovascular response was observed. This finding was corroborated by LFP recordings made in 5 nTG mice where responses to focused PS were similarly absent (Fig. 2a).

Next, we wanted to test whether the focused PS response was driven by blue light and thus ChR2 stimulation, so we contrasted LFP responses to focused 458 nm PS vs. focused 552 nm PS (Fig. 2b). Responses to 458 nm stimulation were 289 ± 23% larger than that to 552 nm, but the response to 552 nm stimulation was detectable (mean LFP 0.5 ± 0.1 mV). The latter is likely due to the nonzero ChR2 excitation cross section at 552 nm (Zhang et al., 2006; Klapoetke et al., 2014), allowing small photocurrents to be induced even at this off-peak wavelength. Additionally, we compared cerebrovascular responses of a single vessel in a TG mouse (Fig. 2d) to 458 nm vs. 552 nm focused PS. While a small signal deflection in response to 552 nm stimulation can be visually observed, it is within the range of baseline fluctuations in RBC speed. These results support the notion that the source of cerebrovascular response to 458 nm in TG animals was neuronal excitation via blue light photoactivation of ChR2.

3.2. Kinetics of cerebrovascular responses in penetrating arterioles and venules

Because penetrating arterioles and venules are integral parts of the cortical microvascular network but serve distinct functions, we explored differences in cortical penetrating arteriolar and venular responses to focused PS (3 mW/mm^2, 130 μm stimulus ROI diameter, 551 ms repetition rate, 4μs/pixel, 2.2s duration, $N_{mice} = 6$, $N_{vessels} = 20$). While response duration in arterioles and venules was found indistinguishable ($p = 0.13$, $duration_{art} = 19 \pm 7s$, $duration_{ven} = 26 \pm 12s$, Fig. 3e), the average absolute Δv_{RBC} ($\Delta v_{RBC\ avg}$ in *mm/s*, Fig. 3c) was significantly higher in arterioles ($p = 2.4x10^{-5}$, $\Delta v_{RBC,art} = 0.41 \pm 0.07$ mm/s, $\Delta v_{RBC,ven} = 0.16 \pm 0.06$ mm/s) while the relative RBC speed change over baseline ($\Delta v_{RBC\ avg}$ in %, Fig. 3d) was higher in venules than in arterioles ($p = 8.0x10^{-4}$, $\Delta v_{RBC,art} = 20 \pm 3\%$, $\Delta v_{RBC,ven} = 48 \pm 19\%$). This is likely due to the half an order of magnitude lower baseline v_{RBC} in venules compared to arterioles (Fig. 3b, $p = 1.2x10^{-5}$, $v_{RBC,art} = 2.0 \pm 0.7$ mm/s, $v_{RBC,ven} = 0.4 \pm 0.2$ mm/s). Furthermore, we compared the absolute and relative accelerations of penetrating arterioles and venules (Fig. 3f and g) and found that arterioles also had higher absolute acceleration (*mm/s^2*, $p = 0.001$, $a_{art} = 0.06 \pm 0.02$ mm/s^2, $a_{ven} = 0.03 \pm 0.01$ mm/s^2) while venules had higher relative acceleration (*%/s*, $p = 5.4x10^{-4}$, $a_{art} = 3.1 \pm 0.6\%/s$, $a_{ven} = 8 \pm 3\%/s$). Of note, the pyramidal soma density in the arteriolar vs. venular focused PS region was indistinguishable, as evaluated by segmentation of the green channel of the stack of 2PFM images acquired in each animal over the superficial 300 μm of the cortical surface (p = 0.61, $\rho_{soma,art} = 11 \pm 6x10^3 mm^{-3}$, $\rho_{soma,ven} = 11 \pm 5x10^3 mm^{-3}$), as displayed in Supplementary Fig. 1.

3.3. Cerebrovascular responses to focused and diffuse photostimulation

Because fiber-delivered diffuse PS is currently the most commonly-employed method of opsin photoactivation (C. K. Kim et al., 2017; Zhang et al., 2010), we investigated the difference in cerebrovascular responses to focused PS (3 mW/mm^2, 130 μm stimulus ROI diameter, 551 ms repetition rate, 4μs/pixel, 5s duration) vs. diffuse PS (8 mW/mm^2, 20Hz, 10 ms pulse length, 5s duration) (Fig. 4, N = 5 mice). While the differences (with respect to the inherent spatiotemporal properties) in these stimulation modalities make a direct comparison difficult, for ease of reference the responses to focal stimulation are reported alongside those to conventional diffuse photostimulation. The parameters of each modality were optimized independently of one

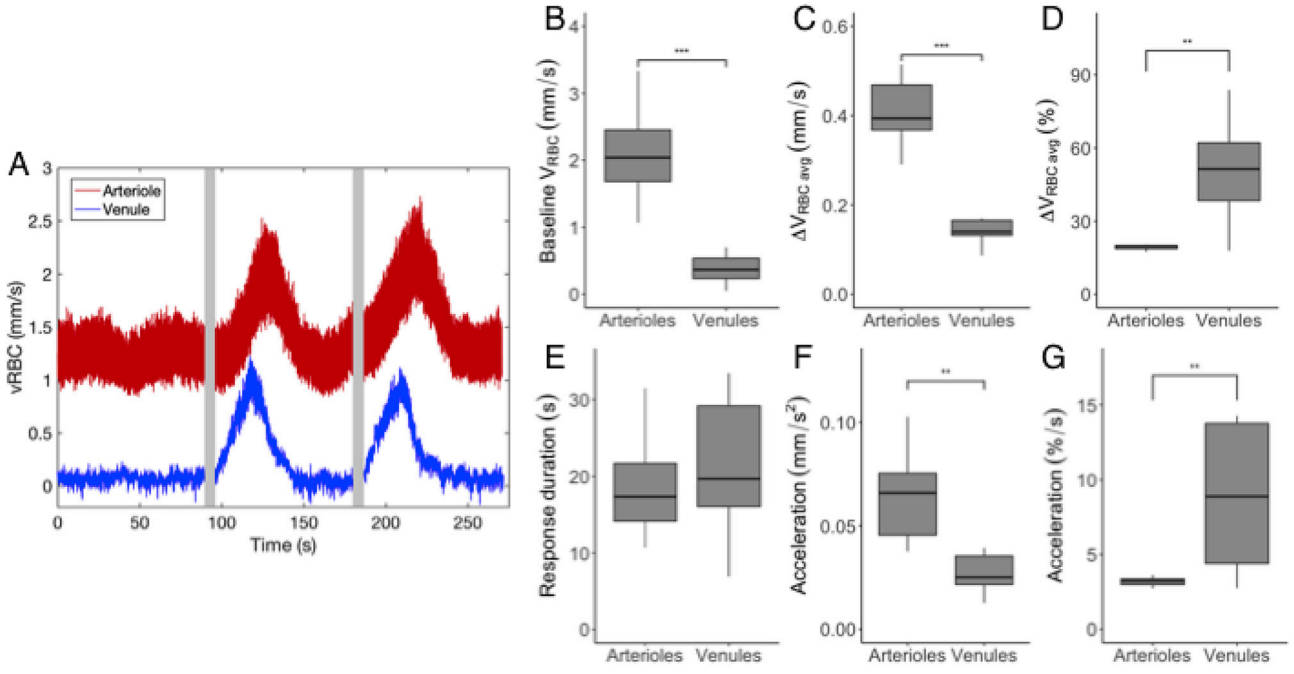

Fig. 3. Arteriolar vs. venular responses to focused optogenetic photostimulation. A. Comparison of arteriolar and venular v_{RBC} response to 458 nm local focused PS (3 mW/mm^2, 130 μm stimulus ROI diameter, 551 ms repetition rate, 4μs/pixel, 2.2s duration). Gray area indicates stimulus duration. B-G. Calculated parameters of individual arteriole and venular v_{RBC} responses. Average parameters of repeated stimulus deliveries in a single recording are plotted (i.e. 5 stimulus deliveries in a single vessel, average parameters of 5 individual responses are plotted). Wilcoxon rank sum test was used to determine if statistically-significant differences exist (***: $p < 0.001$, **: $p < 0.01$, *: $p < 0.05$) and means are reported ± standard deviation (SD). $N_{mice} = 6$, $N_{vessels} = 20$. B. Baseline v_{RBC}. $p = 1.2 \times 10^{-5}$, $mean_{art} = 2.0 \pm 0.7$ mm/s, $mean_{ven} = 0.4 \pm 0.2$ mm/s. C. Average absolute Δv_{RBC}. $p = 2.4 \times 10^{-5}$, $\Delta v_{RBC\ avg,art} = 0.41 \pm 0.07$ mm/s, $\Delta v_{RBC\ avg,ven} = 0.16 \pm 0.06$ mm/s. D. Average relative Δv_{RBC}. $p = 8.0 \times 10^{-4}$, $\Delta v_{RBC\ avg,art} = 20 \pm 3\%$, $\Delta v_{RBC\ avg,ven} = 48 \pm 19\%$. E. Response duration. $p = 0.13$, $duration_{art} = 19 \pm 7$s, $duration_{ven} = 26 \pm 12$s. F. Absolute RBC acceleration (a_{RBC}). $p = 0.001$, $a_{RBC,art} = 0.06 \pm 0.02$ mm/s^2, $a_{RBC,ven} = 0.03 \pm 0.01$ mm/s^2. G. Relative RBC acceleration. $p = 5.4 \times 10^{-4}$, $a_{RBC,art} = 3.1 \pm 0.6\%/s$, $a_{RBC,ven} = 8 \pm 3\%/s$.

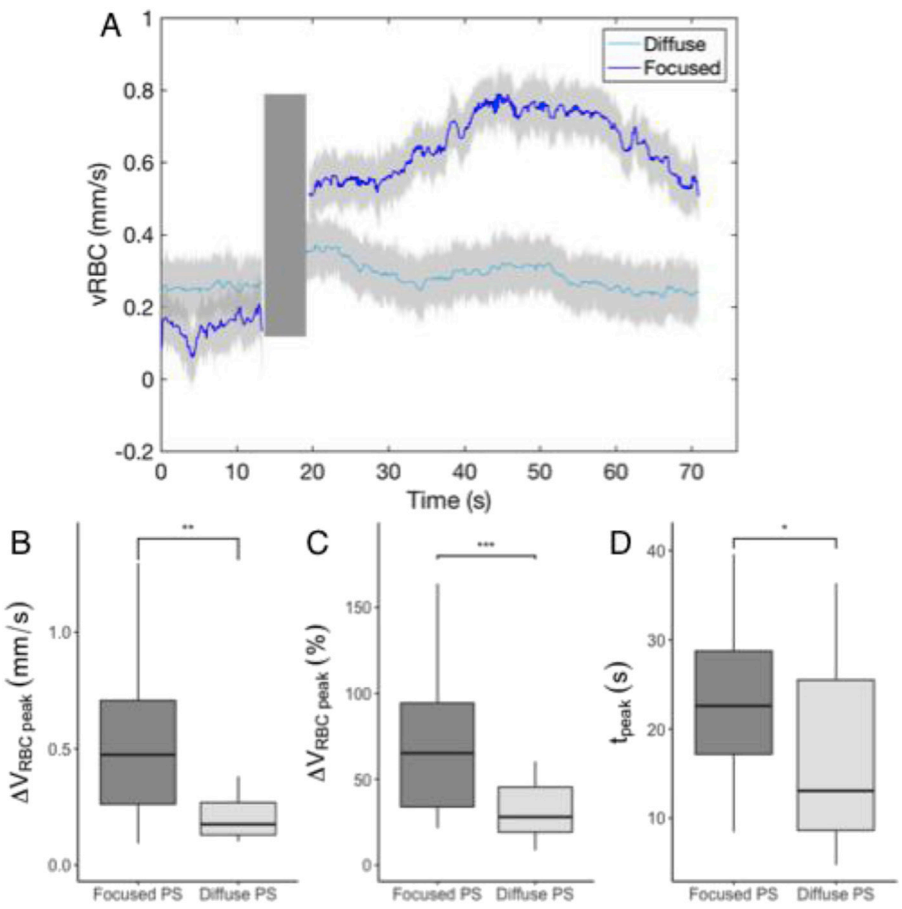

Fig. 4. Cerebrovascular responses to focused vs. diffuse optogenetic photostimulation. A. Representative traces of average v_{RBC} response to 458 nm local focused PS (3 mW/mm^2, 130 µm stimulus ROI diameter, 551 ms repetition rate, 4µs/pixel) and 470 nm fiber-delivered diffuse PS (8 mW/mm^2, 20Hz, 10 ms pulse length) in a single penetrating venule. Dark gray box indicates stimulus duration, light gray shading indicates 95% CI of LSPIV v_{RBC} estimate, coloured traces indicate average v_{RBC} response of 5 stimulus deliveries. B-D. Calculated parameters of individual responses in all penetrating vessels. Average parameters of repeated stimulus deliveries in a single recording are plotted (i.e. 5 stimulus deliveries, average parameters of 5 individual responses are plotted). Wilcoxon rank sum test was used to determine if statistically-significant differences exist (***: $p < 0.001$, **: $p < 0.01$, *: $p < 0.05$) and means are reported ± standard deviation (SD). $N_{mice} = 12$, $N_{vessels} = 57$. B. Peak absolute Δv_{RBC}. $p = 0.002$, $\Delta v_{RBC\ peak,foc} = 0.61 \pm 0.45$ mm/s, $\Delta v_{RBC\ peak,unfoc} = 0.17 \pm 0.08$ mm/s. C. Peak relative Δv_{RBC}. $p = 0.0001$, $\Delta v_{RBC\ peak,foc} = 75 \pm 48\%$, $\Delta v_{RBC\ peak,unfoc} = 35 \pm 23\%$. D. t_{peak}. $p = 0.024$, $t_{peak,foc} = 23 \pm 8$s, $t_{peak,unfoc} = 18 \pm 10$s.

another within the context of our experimental setup (i.e. maximal response yield at low light power levels and minimal duration of the return to baseline). Even with comparable power of diffuse PS, focused PS elicited larger peak absolute v_{RBC} changes across both vessel types (Fig. 4b, $p = 0.002$, $\Delta v_{RBC,foc} = 0.61 \pm 0.45$ mm/s, $\Delta v_{RBC,unfoc} = 0.17 \pm 0.08$ mm/s), larger peak relative v_{RBC} changes (Fig. 4c, $p = 0.0001$, $\Delta v_{RBC,foc} = 75 \pm 48\%$, $\Delta v_{RBC,unfoc} = 35 \pm 23\%$), and longer peak times (Fig. 4d, $p = 0.024$, $t_{peak,foc} = 23 \pm 8$s, $t_{peak,unfoc} = 18 \pm 10$s). Of

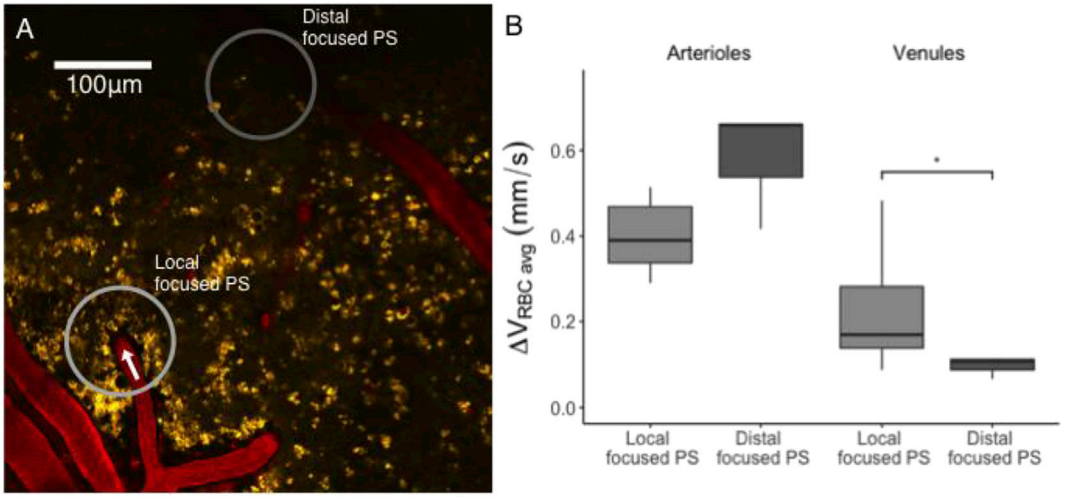

Fig. 5. Cerebrovascular response dependence on focused optogenetic photostimulation region location. A. 2PFM XY image of Texas Red-labeled superficial penetrating vessels near the cortical surface (red) and ChR2-YFP-expressing pyramidal neurons (yellow). Light gray and dark gray circles represent local and distal focused PS stimulation ROIs respectively (2 mW/mm^2, 130 µm stimulus ROI diameter, 551 ms repetition rate, 4µs/pixel, 2.2s duration). B. Comparison of average absolute Δv_{RBC} in arterioles and venules when using local focused PS (over vessel) and distal focused PS (300 µm away from vessel). Average parameters of repeated stimulus deliveries in a single recording are plotted (i.e. 5 stimulus deliveries in a single vessel, average parameters of 5 individual responses are plotted). Wilcoxon rank sum test was used to determine if statistically-significant differences exist (***: $p < 0.001$, **: $p < 0.01$, *: $p < 0.05$) and means are reported ± standard deviation (SD). $N_{mice} = 10$, $N_{vessels} = 45$. B. $p_{art} = 0.21$ ($\Delta v_{RBC\ avg,art,local} = 0.5 \pm 0.3$ m/s, $\Delta v_{RBC\ avg,art,distal} = 0.7 \pm 0.3$ m/s), $p_{ven} = 0.017$ ($\Delta v_{RBC\ avg,ven,local} = 0.2 \pm 0.1$ m/s, $\Delta v_{RBC\ avg,ven,distal} = 0.13 \pm 0.09$ m/s).

note, these responses to the diffuse PS are also consistent with previous work (Uhlirova et al., 2016; Chen et al., 2012; Iordanova et al., 2015). Moreover, the response yields were higher for focused PS: 73 ± 10% (291/395 stimulus presentations across 12 mice) for focused PS and 42 ± 29% (57/137 stimulus presentations across 5 mice) for diffuse PS, p = 0.03. Supplementary Fig. 2 shows the dependence of cerebrovascular response magnitude on intensity of focused PS vs. diffuse PS. No intensity-dependence is seen for focused PS (likely due to a saturation effect), whereas roughly linear dependence is seen with diffuse PS.

3.4. Effects of ROI location on cerebrovascular responses to focused photostimulation

We also examined the effect of the location of PS region on the cerebrovascular responses, thus contrasting over-vessel (local) versus away-from-vessel (distal) focused PS (Fig. 5, $N_{mice} = 10$, $N_{vessels} = 45$, 2 mW/mm^2, 130 μm stimulus ROI diameter, 551 ms repetition rate, 4μs/pixel, 2.2s duration). We found that $\Delta v_{RBC,avg}$ in venules was significantly reduced by distal vs. local focused PS ($p = 0.017$, $\Delta v_{RBC,avg,local} = 0.2 \pm 0.1$ mm/s, $\Delta v_{RBC,avg,distal} = 0.13 \pm 0.09$ m/s) whereas arteriolar $\Delta v_{RBC,peak}$ was not statistically affected by stimulus location ($p = 0.21$, $\Delta v_{RBC,peak,local} = 0.5 \pm 0.3$ m/s, $\Delta v_{RBC,peak,distal} = 0.7 \pm 0.3$ m/s), indicating a difference in the arteriolar and venular territories. This result was further supported by the aforementioned lack of difference in the soma density in the arteriolar vs. venular PS ROIs.

3.5. Neuronal responses to optogenetic and physiological stimulations

We next tested whether focused PS evokes cerebrovascular responses via local neuronal activation, as opposed to other effects that may circumvent normal neurovascular signaling (Rungta et al., 2017). Local field potential (LFP) recordings were obtained in a separate group of animals ($N_{mice} = 6$) to examine the neuronal response to focused PS and compare it with diffuse PS as well as sensory (whisker) stimulation. Fig. 6a and b displays representative LFP recordings of responses to focused PS (3 mW/mm^2, 130 μm stimulus ROI diameter, 551 ms repetition rate, 4μs/pixel) compared to diffuse PS (8 mW/mm^2, 20Hz, 10 ms pulse length) and whisker stimulation (air puff). LFP responses to whisker stimulation were indistinguishable from those to focused PS (Fig. 6c), ($p = 0.62$, $\Delta LFP_{foc} = 1.6 \pm 0.8$ mV, $\Delta LFP_{whis} = 2.9 \pm 2.7$ mV), but the variability of the whisker responses across subjects was much larger than that to focused PS large ($SD_{whis} = 2.7$ mV vs. $SD_{foc} = 0.8$ mV, Fig. 6c). LFP responses to focused PS were also larger than the LFP responses to PS ($p = 0.05$, $\Delta LFP_{foc} = 1.6 \pm 0.8$ mV, $\Delta LFP_{unfoc} = 1.1 \pm 0.7$ mV), which is in line with the respective cerebrovascular response magnitudes. The timing parameters (Fig. 6d and e) for the optogenetic stimulation

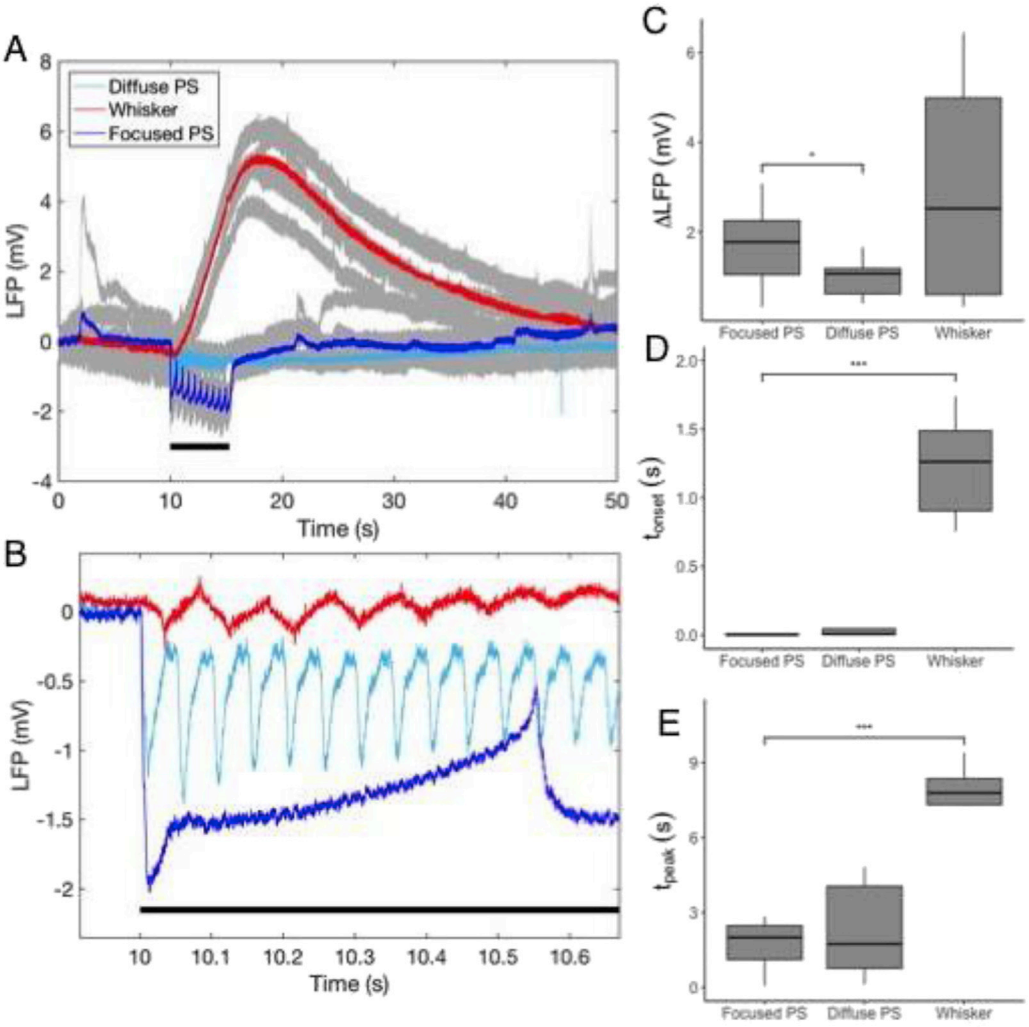

Fig. 6. Neuronal responses to optogenetic photostimulation vs. whisker puff stimulation. A. Representative traces of local field potential (LFP) recordings in Thy1-ChR2 mice in response to 458 nm local focused photostimulation (PS) (3 mW/mm^2, 130 μm stimulus ROI diameter, 551 ms repetition rate, 4μs/pixel), 470 nm fiber-delivered diffuse PS (8 mW/mm^2, 20Hz, 10 ms pulse length), and whisker puff stimulation (10Hz). Gray indicates individual traces, coloured traces depict average response to stimulation, black bar indicates stimulus duration. B. Expanded temporal axis of representative traces showing evoked potentials post stimulus onset. C-E. Calculated parameters of individual LFP responses. Average parameters of repeated stimulus deliveries in a single recording are plotted (i.e. 5 stimulus deliveries, average parameters of 5 individual responses are plotted). Wilcoxon rank sum test was used to determine if statistically-significant differences exist (***: $p < 0.001$, **: $p < 0.01$, *: $p < 0.05$) and means are reported ± standard deviation (SD). $N_{mice} = 6$, Focused PS N = 15, Diffuse PS = 13, Whisker = 6. B. Peak LFP amplitude. $p_{Focused\ PS/Whisker} = 0.62$ ($\Delta LFP_{foc} = 1.6 \pm 0.8$ mV, $\Delta LFP_{whis} = 2.9 \pm 2.7$ mV), $p_{Focused\ PS/Diffuse\ PS} = 0.05$ ($\Delta LFP_{foc} = 1.6 \pm 0.8$ mV, $\Delta LFP_{unfoc} = 1.1 \pm 0.7$ mV). C. t_{onset}. $p_{Focused\ PS/Whisker} = 3.7 \times 10^{-5}$ ($t_{onset,foc} = 0.01 \pm 0.01$s, $t_{onset,whis} = 1.2 \pm 0.4$s), $p_{Focused\ PS/Diffuse\ PS} = 0.25$ ($mean_{foc} = 0.01 \pm 0.01$s, $mean_{unfoc} = 0.1 \pm 0.2$s). D. t_{peak}. $p_{Focused\ PS/Whisker} = 3.6 \times 10^{-5}$ ($t_{peak,foc} = 2.2 \pm 1.7$s, $t_{peak,whis} = 7.7 \pm 1.3$s), $p_{Focused\ PS/Diffuse\ PS} = 1$ ($t_{peak,foc} = 2.2 \pm 1.7$s, $t_{peak,unfoc} = 2.3 \pm 1.7$s).

modalities were not significantly different ($p_{tonset} = 0.25$: $t_{onset,foc} = 0.01 \pm 0.01s$, $t_{onset,unfoc} = 0.1 \pm 0.2s$; $p_{tpeak} = 0.997$: $t_{peak,foc} = 2.2 \pm 1.7s$, $t_{peak,unfoc} = 2.3 \pm 1.7s$), but whisker stimulation responses were significantly longer than those of either PS modalities ($p_{tonset} = 3.7x10^{-5}$: $t_{onset,foc} = 0.01 \pm 0.01s$, $t_{onset,whis} = 1.2 \pm 0.4s$; $p_{tpeak} = 3.6x10^{-5}$: $t_{peak,foc} = 2.2 \pm 1.7s$, $t_{peak,whis} = 7.7 \pm 1.3s$). Cerebrovascular responses to whisker stimulation are summarized in Supplementary Fig. 3.

4. Discussion

While a range of modalities have been used to explore neurovascular coupling in pathophysiological contexts, 2PFM in combination with optogenetics grants the unique opportunity to map brain activation at high spatio-temporal resolution and in a neuronal subpopulation specific manner. While ChR2 activation induced neurovascular coupling was investigated in several studies (Scott and Murphy, 2012; Iordanova et al., 2015, 2018; Uhlirova et al., 2016; Cheng et al., 2014; Anenberg et al., 2015; Rungta et al., 2017; Richner et al., 2015; Bauer et al., 2018; Vazquez et al., 2014), the extent of the advantages afforded by spatiotemporal manipulation of stimulation light has not been fully characterized. ChR2 photoactivation in Thy1-ChR2 mice has been shown to elicit transient increases in glucose metabolism (Richner et al., 2015). Recent work underscored the role of interneurons in neurovascular coupling: photoactivation of ChR2 expressing interneurons in VGAT-ChR2 mice increased cerebral blood flow despite the overall decrease in local neuronal activity; a response shown unaffected by blockage of ionotropic glutamatergic or GABAergic synaptic transmission (Anenberg et al., 2015). Further cellular specificity of the neurovascular coupling was shown by demonstrating Neuropeptide Y dependent constriction with photoactivation of ChR2 in interneurons in the VGAT-ChR2 mice (Uhlirova et al., 2016). Half an order of magnitude larger and twice as rapid ChR2 photoactivation-induced dilations in pial arteries vs. veins in Thy1-ChR2 mice have been reported (Richner et al., 2015). Additionally, neurovascular coupling elicited by photoactivation of ChR2 in the cortical forelimb area was found largely conformant to that elicited in the same area by electrical stimulation of the forelimb (Iordanova et al., 2015). Despite differences in the ChR2 expression mechanism as well as anesthesia protocol, we presently observed comparable diffuse PS-elicited cerebrovascular responses to those reported earlier (Iordanova et al., 2015) (~50% CBF increase via LDF recording vs. 35 ± 23% in single vessels in this work). Our diffuse PS-elicited LFP magnitudes are also in agreement with prior reports (Iordanova et al., 2015; Zhang et al., 2010; Patterson et al., 2013).

Recent work by (Rungta et al., 2017) suggested that diffuse blue light delivered with an optical fiber may exert direct, light energy-dependent effects on cerebrovasculature of wild-type animals, in contrast to the lack of such effects in wild-type animals in other work (Uhlirova et al., 2016) and in the current study. The present study used alpha-chloralose (vs. ketamine-xylazine or isoflurane) anesthesia and 10 ms, 20Hz, 8 mW/mm^2, 2–5s (vs. 20 ms, 20 Hz, 5 mW, 2s) diffuse PS, although it is at present unclear how these methodological differences would account for the discrepant findings. While we observed no responses in our control experiments, the work done by (Rungta et al., 2017) reinforces the necessity for appropriate controls in optogenetic studies.

The diffuse PS results in simultaneous illumination of the entire exposed area of the cortex (~4 mm^2) down to a depth of 200 μm, hence recruiting thousands of cell bodies. In contrast, the focused PS excites ~1/100th the volume of tissue (~0.002 mm^3 with 200 μm depth of penetration) containing ~2 orders of magnitude fewer neurons; further, raster scanning over this region results in sequential illumination of cortical columns and thus asynchronous activation of neurons. The smaller number of neurons and the asynchronous activation may lead to a more physiologically-pertinent pattern of neuronal activity and hence larger cerebrovascular responses to focused PS when compared to those of diffuse PS. The higher variability of diffuse PS is likely due to the pathophysiological synchrony imposed thereby on a large number of pyramidal neurons across an extensive area of the cortex (Houben et al., 2017). Given that LFP receptive fields are around 250 μm^2 in the cortex (Xing et al., 2009), only a limited portion of tissue excited by diffuse PS will participate in the LFP signal, resulting in local LFP recorded responses being comparable in magnitude. Notably, whisker stimulation also leads to "asynchronous" neuronal response. With the exception of a few prior studies with in-plane spatial restriction of 100–200 μm of the photostimulation ROI via beam collimation (Wilson et al., 2013; Anenberg et al., 2015; Uhlirova et al., 2016; Scott and Murphy, 2012), the majority of studies to date used whole-field stimulation (~mm^2 range) of the brain cortex. The optimization of the photostimulation paradigm to the application has not been systematically done hitherto.

In the current work, we measured the neurovascular effects of PS through RBC speed changes. We explored the option of performing a "cross" trajectory (Shih et al., 2012) to assess both RBC speed and vessel diameter, but found that the decreased sampling frequency compromised RBC speed estimation in faster flow arterioles. Also, we have previously found point measurements of vessel diameter of limited use for predicting vessel volume changes, likely resulting from highly heterogeneous distribution of the contractile elements along the length of non-arteriolar vessels (Lindvere et al., 2013).

We demonstrated that focused PS affords important advantages over fiber-delivered diffuse PS when studying either neuronal excitability or cerebrovascular reactivity. At comparable light intensities, evoked potentials (measured on intracerebral LFP) were found to be of similar duration but ~40% higher magnitude than those measured in response to conventionally used diffuse PS. These neuronal responses were stable in magnitude on stimulus repetition, suggesting a lack of thermal effects. Cerebrovascular responses (assayed by changes in RBC speed in individual cortical penetrating vessels) to focused PS were twice the amplitude and ~30% longer than those seen in response to diffuse PS. We speculate that this difference is due to the attenuation of the electrical conduction along the endothelium (Tran et al., 2012) that is present with whisker stimulation and with diffuse photostimulation - as these stimuli engage multiple vessels - in contrast to the focused photostimulation where an endothelium of only one vessel is directly affected. The matching LDF responses recorded by the 480 μm diameter LDF probe are the result of the LDF signal reflecting net RBC flow changes across a set of neighbouring penetrating vessels (arteries and venules); i.e. the modulatory effect of the cortical vascular network as a whole is again at play, temporally restricting the response. Indeed, we have previously reported using 2PFM in wild type rodents (rats) that the individual vessel responses (Lindvere et al., 2013) are much more heterogeneous than what's predicted by the averaged, regional vascular response; and other groups have, using 2PFM, also reported on long lasting responses in individual vessels to prolonged stimulation (Hill et al., 2015). Moreover, cerebrovascular responses to repeated focused PS showed less inter-trial variation than did the responses to conventional diffuse PS. The higher SNR of focused vs. diffuse PS confers a significant advantage in the study of disease models, particularly those exhibiting spatially specific alterations in neurovascular coupling such as ischemia and traumatic brain injury. In these cases, focused PS enables investigation of injury as a function of distance from the lesion core.

Focused PS generated less variable relative responses when positioned over the arterioles than over the venules, supporting the notion of stimulation-induced arteriolar dilation being proportional to their resting tone (Drew et al., 2011). Furthermore, cerebrovascular response amplitude was not affected by photostimulation ROI movement of 300 μm (Fig. 5) as both fall within the arterioles vascular territory (350 μm radially in the mouse neocortex (Nishimura et al., 2007)). In contrast, venules' average responses were attenuated during distal vs. proximal photostimulation as the former falls outside the vascular territory of a given cortical penetrating venule. Stimulating the parenchymal territory specific to the vessel under examination enables neurovascular coupling interrogation by functional unit, reducing variability and allowing spatial

mapping of the pathological disturbance. This method is also applicable to custom fluorescence microscopy configurations in that the main components required are a diode laser, XY-galvanometers, and the appropriate beam-combining optics (Fig. 1).

The ability of the raster scan photostimulation to isolate the penetrating vessel's territories suggests that unlike diffuse PS, focused PS may resolve cortical vascular functional units, while still engaging on the order of 50 neurons (as estimated from the structural scan shown in Supplementary Fig. 1). For the photostimulation-driven response to be restricted to single units, the photostimulation needs to involve the two-photon fluorescence excitation process. However, preliminary experiments using the second Ti:Sapphire laser on our microscopy platform (data not shown) revealed serious limitations of the concurrent two-photon photoexcitation and imaging. In particular, two-photon fluorescence photoexcitation (limited in power to avoid damage to the cell) was found to elicit very small neuronal currents, whose detection required cell-attached recordings. Few such recordings could be done in an animal due to the invasive nature of the recording. Although calcium reporters present a potentially non-invasive route of imaging single unit responses, their use is confounded by the strong artifacts generated by photostimulation in the detectors and their slow kinetics being challenged to resolve neuronal firing. Moreover, as spatial gradients of pathological changes in the neurovascular signaling elicited by injury (e.g. ischemia) may be of much lower spatial frequency, the cerebrovascular response may be a better assay for their assessment than are the (sparse) measurements of changes in excitability of individual neurons.

As with most 2PFM studies, the primary limitation of this work is in the extent of the cortical depth perturbed and interrogated. The cerebrovascular measurements in deeper layers are of particular interest given the relative density of cortical layers and the layer-wise processing pattern of physiological stimulation (Li et al., 2011; J. Wu et al., 2016). However, light illumination from the top of the brain surface elicits initial perturbation in the superficial neuronal processes, thus inverting the physiological processing cascade (here seen in the opposite polarity of LFP to whisker stimulation vs. either focused PS or diffuse PS). Notwithstanding the advantages of focused PS in the current work, diffuse PS is clearly better suited to chronic applications in freely behaving animals.

Of note, we did not observe RBC speed changes in response to whisker stimulation despite the increases in RBC flow measured with Laser Doppler Flowmetry (LDF) (Supplementary Fig. 3) and LFP recorded on electrophysiology (Fig. 6). We suspect this failure arose due to the differences in spatial flow redistribution at the microscopic scale in response to whisker puff vs. photostimulation. In addition, hardware limitations in our setup precluded us from matching the wavelengths used for focused vs. diffuse PS. For this reason along with the aforementioned spatiotemporal differences inherent to the two PS modalities, a direct comparison between focused and diffuse PS is not possible here. In order to have a more thorough understanding of the underlying differences between the two photostimulation modalities, comprehensive variations on the parameters of each modality should be performed and with that more concrete conclusions could be made. Nonetheless, the data presented here would be a good starting point for such studies further exploring the applications of focused PS. However, earlier studies performed on the variant of ChR2 used in this study (Lin et al., 2009; Nagel et al., 2003; Bamann et al., 2008; Prigge et al., 2012) indicate that over the wavelength range of 458–470 nm, the excitation cross-spectrum shows very little variation (2–3%): the distinctions we see in the respective responses are thus likely not due to the difference in the PS wavelengths but a result of the different spatiotemporal properties of the two PS modalities. Notwithstanding, careful reporting of the photostimulation parameters (frequency, pulse duration, duty cycle, and light intensity at brain surface) is key, along with characterization of responses' dependence on input power, which likely depends on the anesthesia protocol (Masamoto et al., 2007; Rungta et al., 2017; Paasonen et al., 2018). Notably in the current study, we did not observe a dependence of the cerebrovascular response magnitude on focused PS power (Supplementary Fig. 2): we speculate that the powers examined induced increases in metabolic demand at the point of saturation within the excitation volume. This point likely also contributes to the fact that the responses to focused PS presented in this study are dissimilar in terms of magnitude and duration to some physiological responses as well as optogenetically-evoked vascular responses in other studies where the responses to PS and physiological stimuli are more aligned (Vazquez et al., 2014; Bauer et al., 2018; Iordanova et al. 2015, 2018; Scott and Murphy, 2012). On a final methodological note, we observed a difference between arterioles and venules with respect to absolute vs. relative v_{RBC} changes in response to stimuli. Consequently, studies using a relative measure of the cerebrovascular reactivity will be venule weighted and so should take into account the differences in the relative density of penetrating venules and arterioles among cortical regions (Lee et al., 2001).

In summary, the present work introduced focused photostimulation of the channelrhodopsin-expressing pyramidal neurons in barrel cortex of Thy1-ChR2 mice as a means to interrogate neurovascular coupling. Our stimulation paradigm is shown to elicit longer cerebrovascular responses of twice the magnitude of those seen in response to diffuse photostimulation with comparable evoked local field potentials. Additionally, focused photostimulation provided ~65% higher yield of cerebrovascular responses in this experiment as well as a doubling of signal-to-noise ratio. While these stimulation modalities have inherently different spatiotemporal properties, our data reveal important advantages of focused optogenetic photoactivation for examination of spatially specific brain pathologies affecting cortical microcirculation. Focused photostimulation can be easily integrated into fluorescence microscopy platforms as a means of assessing neuronal excitability and cerebrovascular reactivity in health and disease.

Declarations of interest

None.

Funding

This work was supported by grants from the Canadian Institutes of Health Research and the Natural Sciences and Engineering Research Council of Canada.

Appendix A. Supplementary data

Supplementary data to this article can be found online at https://doi.org/10.1016/j.neuroimage.2019.01.036.

References

Al-Juboori, Saif I., Dondzillo, Anna, Stubblefield, Elizabeth A., Felsen, Gidon, Lei, Tim C., Klug, Achim, 2013. Light Scattering Properties Vary across Different Regions of the Adult Mouse Brain. PLoS One 8 (7), e67626.

Anenberg, Eitan, Chan, Allen W., Xie, Yicheng, LeDue, Jeffrey M., Murphy, Timothy H., 2015. Optogenetic stimulation of GABA neurons can decrease local neuronal activity while increasing cortical blood flow. J. Cerebr. Blood Flow Metabol.: Offic. J. Int. Soc. Cereb. Blood Flow Metabol. 35 (10), 1579–1586.

Arenkiel, Benjamin R., Peca, Joao, Davison, Ian G., Feliciano, Catia, Deisseroth, Karl, Augustine, George J., Ehlers, Michael D., Feng, Guoping, 2007. In vivo light-induced activation of neural circuitry in transgenic mice expressing channelrhodopsin-2. Neuron 54 (2), 205–218.

Attwell, David, Iadecola, Costantino, 2002. The neural basis of functional brain imaging signals. Trends Neurosci. 25 (12), 621–625.

Ayling, Oliver G.S., Harrison, Thomas C., Alexander Goroshkov, Jamie D. Boyd, Murphy, Timothy H., 2009. Automated light-based mapping of motor cortex by photoactivation of channelrhodopsin-2 transgenic mice. Nat. Methods 6 (3), 219–224.

Bamann, Christian, Kirsch, Taryn, Nagel, Georg, Bamberg, Ernst, 2008. Spectral characteristics of the photocycle of channelrhodopsin-2 and its implication for channel function. J. Mol. Biol. 375 (3), 686–694.

Bauer, Adam Q., Kraft, Andrew W., Baxter, Grant A., Wright, Patrick W., Reisman, Matthew D., Bice, Annie R., Park, Jasmine J., et al., 2018. Effective connectivity measured using optogenetically evoked hemodynamic signals exhibits

topography distinct from resting state functional connectivity in the mouse. Cerebr. Cortex 28 (1), 370–386.
Boyden, Edward S., Zhang, Feng, Bamberg, Ernst, Nagel, Georg, Deisseroth, Karl, 2005. Millisecond-timescale, genetically targeted optical control of neural activity. Nat. Neurosci. 8 (9), 1263–1268.
Chen, Shangbin, Mohajerani, Majid H., Xie, Yicheng, Murphy, Timothy H., 2012. Optogenetic analysis of neuronal excitability during global ischemia reveals selective deficits in sensory processing following reperfusion in mouse cortex. J. Neurosci.: Offic. J. Soc. Neurosci. 32 (39), 13510–13519.
Cheng, Michelle Y., Wang, Eric H., Woodson, Wyatt J., Wang, Stephanie, Sun, Guohua, Lee, Alex G., Arac, Ahmet, Fenno, Lief E., Deisseroth, Karl, Steinberg, Gary K., 2014. Optogenetic neuronal stimulation promotes functional recovery after stroke. Proc. Natl. Acad. Sci. U. S. A. 111 (35), 12913–12918.
Christie, Isabel N., Wells, Jack A., Paul, Southern, Marina, Nephtali, Kasparov, Sergey, Gourine, Alexander V., Lythgoe, Mark F., 2013. fMRI response to blue light delivery in the naïve brain: implications for combined optogenetic fMRI studies. Neuroimage 66 (February), 634–641.
Davis, T.L., Kwong, K.K., Weisskoff, R.M., Rosen, B.R., 1998. Calibrated functional MRI: mapping the dynamics of oxidative metabolism. Proc. Natl. Acad. Sci. U. S. A. 95 (4), 1834–1839.
Dirnagl, U., Iadecola, C., Moskowitz, M. a., 1999. Pathobiology of ischaemic stroke: an integrated view. Trends Neurosci. 22 (9), 391–397.
Dorr, Adrienne, Sahota, Bhupinder, Chinta, Lakshminarayan V., Brown, Mary E., Lai, Aaron Y., Ma, Keran, Hawkes, Cheryl A., McLaurin, Joanne, Stefanovic, Bojana, 2012. "Amyloid-β-Dependent compromise of microvascular structure and function in a model of alzheimer's disease. Brain: J. Neurol. 135 (Pt 10), 3039–3050.
Drew, Patrick J., Shih, Andy Y., Kleinfeld, David, 2011. Fluctuating and sensory-induced vasodynamics in rodent cortex extend arteriole capacity. Proc. Natl. Acad. Sci. U. S. A. 108 (20), 8473–8478.
Hill, Robert A., Tong, Lei, Peng, Yuan, Murikinati, Sasidhar, Gupta, Shobhana, Grutzendler, Jaime, 2015. Regional blood flow in the normal and ischemic brain is controlled by arteriolar smooth muscle cell contractility and not by capillary pericytes. Neuron 87 (1), 95–110.
Houben, Thijs, Loonen, Inge Cm, Baca, Serapio M., Schenke, Maarten, Meijer, Johanna H., Ferrari, Michel D., Terwindt, Gisela M., et al., 2017. Optogenetic induction of cortical spreading depression in anesthetized and freely behaving mice. J. Cerebr. Blood Flow Metabol.: Offic. J. Int. Soc. Cereb. Blood Flow Metabol. 37 (5), 1641–1655.
Iadecola, Costantino, 2017. The neurovascular unit coming of age: a journey through neurovascular coupling in health and disease. Neuron 96 (1), 17–42.
Iordanova, Bistra, Vazquez, Alberto L., Poplawsky, Alexander J., Fukuda, Mitsuhiro, Kim, Seong-Gi, 2015. Neural and hemodynamic responses to optogenetic and sensory stimulation in the rat somatosensory cortex. J. Cerebr. Blood Flow Metabol.: Offic. J. Int. Soc. Cereb. Blood Flow Metabol. 35 (6), 922–932.
Iordanova, Bistra, Alberto, Vazquez, Kozai, Takashi Dy, Fukuda, Mitsuhiro, Kim, Seong-Gi, 2018. Optogenetic investigation of the variable neurovascular coupling along the interhemispheric circuits. J. Cerebr. Blood Flow Metabol.: Offic. J. Int. Soc. Cereb. Blood Flow Metabol. 38 (4), 627–640.
Jennings, Joshua H., Sparta, Dennis R., Stamatakis, Alice M., Ung, Randall L., Pleil, Kristen E., Kash, Thomas L., Stuber, Garret D., 2013. Distinct extended amygdala circuits for divergent motivational states. Nature 496 (7444), 224–228.
Kim, Tyson N., Goodwill, Patrick W., Chen, Yeni, Conolly, Steven M., Schaffer, Chris B., Liepmann, Dorian, Wang, Rong A., 2012. Line-Scanning Particle Image Velocimetry: an Optical Approach for Quantifying a Wide Range of Blood Flow Speeds in Live Animals. PLoS One 7 (6), e38590. Edited by Timothy W. Secomb.
Kim, Christina K., Adhikari, Avishek, Karl, Deisseroth., 2017. Integration of optogenetics with complementary methodologies in Systems neuroscience. Nat. Rev. Neurosci. 18 (4), 222–235.
Klapoetke, Nathan C., Murata, Yasunobu, Kim, Sung Soo, Pulver, Stefan R., Birdsey-Benson, Amanda, Cho, Yong Ku, Morimoto, Tania K., et al., 2014. Independent optical excitation of distinct neural populations. Nat. Methods 11 (3), 338–346.
Kleinfeld, D., Mitra, P.P., Helmchen, F., Denk, W., 1998. Fluctuations and stimulus-induced changes in blood flow observed in individual capillaries in layers 2 through 4 of rat neocortex. Proc. Natl. Acad. Sci. U. S. A. 95 (26), 15741–15746.
Lammel, Stephan, Lim, Byung Kook, Chen, Ran, Huang, Kee Wui, Betley, Michael J., Tye, Kay M., Deisseroth, Karl, Malenka, Robert C., 2012. Input-specific control of reward and aversion in the ventral tegmental area. Nature 491 (7423), 212–217.
Lauritzen, Martin, 2005. "Reading vascular changes in brain imaging: is dendritic calcium the key?" Nature reviews. Neuroscience 6 (1), 77–85.
Lee, S.P., Duong, T.Q., Yang, G., Iadecola, C., Kim, S.G., 2001. Relative changes of cerebral arterial and venous blood volumes during increased cerebral blood flow: implications for BOLD fMRI. Magn. Reson. Med.: Offic. J. Soc. Magn. Reson. Med.Soc. Magn. Reson. Med. 45 (5), 791–800.
Li, Jennifer, Bravo, Diego S., Louise Upton, A., Gilmour, Gary, Tricklebank, Mark D., Fillenz, Marianne, Martin, Chris, Lowry, John P., Bannerman, David M., McHugh, Stephen B., 2011. Close temporal coupling of neuronal activity and tissue oxygen responses in rodent whisker barrel cortex. Eur. J. Neurosci. 34 (12), 1983–1996.
Lin, John Y., Lin, Michael Z., Paul, Steinbach, Tsien, Roger Y., 2009. Characterization of engineered channelrhodopsin variants with improved properties and kinetics. Biophys. J. 96 (5), 1803–1814.
Lindvere, Liis, Janik, Rafal, Adrienne Dorr, Chartash, David, Sahota, Bhupinder, Sled, John G., Stefanovic, Bojana, 2013. Cerebral microvascular network geometry changes in response to functional stimulation. Neuroimage 71 (May), 248–259.
Masamoto, Kazuto, Kim, Tae, Fukuda, Mitsuhiro, Wang, Ping, Kim, Seong-Gi, 2007. Relationship between neural, vascular, and BOLD signals in isoflurane-anesthetized rat somatosensory cortex. Cerebr. Cortex 17 (4), 942–950.
Nagel, Georg, Szellas, Tanjef, Huhn, Wolfram, Kateriya, Suneel, Adeishvili, Nona, Berthold, Peter, Doris, Ollig, Hegemann, Peter, Bamberg, Ernst, 2003. Channelrhodopsin-2, a directly light-gated cation-selective membrane channel. Proc. Natl. Acad. Sci. U. S. A. 100 (24), 13940–13945.
Nagel, Georg, Brauner, Martin, Liewald, Jana F., Adeishvili, Nona, Bamberg, Ernst, Gottschalk, Alexander, 2005. Light activation of channelrhodopsin-2 in excitable cells of Caenorhabditis elegans triggers rapid behavioral responses. Curr. Biol.: CB 15 (24), 2279–2284.
Nishimura, Nozomi, Schaffer, Chris B., Friedman, Beth, Lyden, Patrick D., Kleinfeld, David, 2007. Penetrating arterioles are a bottleneck in the perfusion of neocortex. Proc. Natl. Acad. Sci. U. S. A. 104 (1), 365–370.
Paasonen, Jaakko, Stenroos, Petteri, Salo, Raimo A., Kiviniemi, Vesa, Gröhn, Olli, 2018. Functional connectivity under six anesthesia protocols and the awake condition in rat brain. Neuroimage 172 (May), 9–20.
Patterson, Michael Andrew, Lagier, Samuel, Carleton, Alan, 2013. Odor representations in the olfactory bulb evolve after the first breath and persist as an odor afterimage. Proc. Natl. Acad. Sci. U. S. A. 110 (35), E3340–E3349.
Prigge, Matthias, Schneider, Franziska, Tsunoda, Satoshi P., Shilyansky, Carrie, Wietek, Jonas, Deisseroth, Karl, Hegemann, Peter, 2012. Color-tuned channelrhodopsins for multiwavelength optogenetics. J. Biol. Chem. 287 (38), 31804–31812.
Richner, Thomas J., Ryan, Baumgartner, Brodnick, Sarah K., Azimipour, Mehdi, Krugner-Higby, Lisa A., Eliceiri, Kevin W., Williams, Justin C., Pashaie, Ramin, 2015. Patterned optogenetic modulation of neurovascular and metabolic signals. J. Cerebr. Blood Flow Metabol.: Offic. J. Int. Soc. Cereb. Blood Flow Metabol. 35 (1), 140–147.
Rungta, Ravi L., Osmanski, Bruno-Félix, Boido, Davide, Tanter, Mickael, Charpak, Serge, 2017. Light controls cerebral blood flow in naive animals. Nat. Commun. 8 (January), 14191.
Scott, Nadia A., Murphy, Timothy H., 2012. Hemodynamic Responses Evoked by Neuronal Stimulation via Channelrhodopsin-2 Can Be Independent of Intracortical Glutamatergic Synaptic Transmission. PLoS One 7 (1), e29859.
Shih, Andy Y., Driscoll, Jonathan D., Drew, Patrick J., Nishimura, Nozomi, Schaffer, Chris B., Kleinfeld, David, 2012. Two-photon microscopy as a tool to study blood flow and neurovascular coupling in the rodent brain. J. Cerebr. Blood Flow Metabol.: Offic. J. Int. Soc. Cereb. Blood Flow Metabol. 32 (7), 1277–1309.
Tran, Cam Ha T., Vigmond, Edward J., Goldman, Daniel, France, Plane, Welsh, Donald G., 2012. Electrical communication in branching arterial networks. Am. J. Physiol. Heart Circ. Physiol. 303 (6), H680–H692.
Uhlirova, Hana, Kıvılcım, Kılıç, Tian, Peifang, Martin, Thunemann, Desjardins, Michèle, Saisan, Payam A., Sava, Sakadžić, et al., 2016. Cell type specificity of neurovascular coupling in cerebral cortex. eLife 5 (May). https://doi.org/10.7554/eLife.14315.
Vazquez, Alberto L., Fukuda, Mitsuhiro, Crowley, Justin C., Kim, Seong-Gi, 2014. Neural and hemodynamic responses elicited by forelimb- and photo-stimulation in channelrhodopsin-2 mice: insights into the hemodynamic point spread function. Cerebr. Cortex 24 (11), 2908–2919.
Wilson, Nathan R., Schummers, James, Runyan, Caroline a., Yan, Sherry X., Chen, Robert E., Deng, Yuting, Sur, Mriganka, 2013. Two-way communication with neural networks in vivo using focused light. Nat. Protoc. 8 (6), 1184–1203.
Wu, Guang-Yan, Liu, Guo-Long, Zhang, Hui-Min, Chen, Chong, Liu, Shu-Lei, Feng, Hua, Sui, Jian-Feng, 2015. Optogenetic stimulation of mPFC pyramidal neurons as a conditioned stimulus supports associative learning in rats. Sci. Rep. 5 (May), 10065.
Wu, Jingpeng, Guo, Congdi, Chen, Shangbin, Jiang, Tao, He, Yong, Ding, Wenxiang, Yang, Zhongqin, Luo, Qingming, Gong, Hui, 2016. Direct 3D analyses reveal barrel-specific vascular distribution and cross-barrel branching in the mouse barrel cortex. Cerebr. Cortex 26 (1), 23–31.
Xing, Dajun, Yeh, Chun-I., Shapley, Robert M., 2009. Spatial spread of the local field potential and its laminar variation in visual cortex. J. Neurosci.: Offic. J. Soc. Neurosci. 29 (37), 11540–11549.
Zhang, Feng, Wang, Li-Ping, Boyden, Edward S., Deisseroth, Karl, 2006. Channelrhodopsin-2 and optical control of excitable cells. Nat. Methods 3 (10), 785–792.
Zhang, Feng, Gradinaru, Viviana, Adamantidis, Antoine R., Durand, Remy, Airan, Raag D., de Lecea, Luis, Deisseroth, Karl, 2010. Optogenetic interrogation of neural circuits: Technology for probing mammalian brain structures. Nat. Protoc. 5 (3), 439–456.